

D-VDAMP: DENOISING-BASED APPROXIMATE MESSAGE PASSING FOR COMPRESSIVE MRI

Christopher A. Metzler, Gordon Wetzstein

Department of Electrical Engineering at Stanford University
{cmetzler, gordon.wetzstein}@stanford.edu

ABSTRACT

Plug and play (P&P) algorithms iteratively apply highly optimized image denoisers to impose priors and solve computational image reconstruction problems, to great effect. However, in general the “effective noise”, that is the difference between the true signal and the intermediate solution, within the iterations of P&P algorithms is neither Gaussian nor white. This fact makes existing denoising algorithms suboptimal.

In this work, we propose a CNN architecture for removing colored Gaussian noise and combine it with the recently proposed VDAMP algorithm, whose effective noise follows a predictable colored Gaussian distribution. We apply the resulting denoising-based VDAMP (D-VDAMP) algorithm to variable density sampled compressive MRI where it substantially outperforms existing techniques.

Index Terms— Compressive Sensing, MRI, Approximate Message Passing, Plug and Play, Denoising

1. INTRODUCTION

The goal of computational imaging (CI) is to recover a vectorized image $\mathbf{x}_o \in \mathbb{C}^n$ from a measurement \mathbf{y} . For the special case of compressive magnetic resonance imaging (MRI), which is one of the more mature and important applications of CI, the forward model can be approximated by

$$\mathbf{y} = \mathbf{M}_\Omega (\mathbf{F}\mathbf{x}_o + \epsilon), \quad (1)$$

where $\mathbf{F} \in \mathbb{C}^{n \times n}$ is a 2-D discrete Fourier transform matrix, $\mathbf{M}_\Omega \in \mathbb{R}^{n \times n}$ is a diagonal matrix, parameterized by $\Omega \in \mathbb{R}^n$, that models subsampling the Fourier coefficients, and ϵ represents complex circular Gaussian distributed noise. The elements $\mathbf{M}_{i,i}$ are one if $\Omega_i = 1$ and zero otherwise. There are $m \ll n$ non-zero elements in Ω .

The quality of any CI imaging system, including MRI, depends on its recovery algorithm. In the last two decades, dozens of CI recovery algorithms have been developed. Among them, plug and play (P&P) approaches [1, 2, 3, 4], which iteratively apply a denoising algorithm to impose a

prior on the reconstruction, have generally been the most successful. P&P approaches using convolutional neural networks (CNNs) have been particularly effective [5]. For a comprehensive review of plug and play methods applied to compressive MRI see [6].

Denoising-based approximate message passing (D-AMP) [3, 7, 8] is an especially exciting P&P algorithm. It converges much faster than competing algorithms and comes with a *scalar* state evolution framework that allows one to predict and reason about its performance. These strengths are a result of a property unique to AMP algorithms: The difference between the ground truth signal and the intermediate reconstructions in AMP, a term known as the “effective noise”, can be modeled as additive *white* Gaussian noise with a known variance [7].

However, like the AMP algorithm on which it is based, for this property to hold D-AMP requires that the elements of the forward operator/measurement matrix follow an i.i.d. sub-Gaussian distribution. When the elements of the matrix are not i.i.d. sub-Gaussian distributed, the effective noise is not white, the state evolution framework does not predict the reconstruction accuracy, and the performance of the algorithm suffers [9, 10].

Much work has gone into extending AMP to work with other measurement matrices. Through the use of damping [9], sequential updates [10, 11], variable splitting [12], and divergence-free denoisers [13], AMP can be extended to work with a far broader class of matrices. However, none of the aforementioned extensions fully support Fourier measurements, which are arguably the most important CS measurement operator. As a result, to date AMP’s performance on Fourier-based CS problems like MRI has been underwhelming [14].

Recently, Millard et al. [15] proposed a novel extension to AMP, coined variable density AMP (VDAMP), in which the reconstruction is produced and predicted on a per wavelet subband basis (related ideas were proposed in [16]). Under this model, the effective noise at each iteration is additive *colored* Gaussian noise with a covariance matrix which is diagonal when the noise is represented in the wavelet domain. Moreover, VDAMP comes with a (weak) *vector* state evolution framework that can predict the variance of the effective noise in each subband, even when dealing with Fourier mea-

C.M. was supported by an appointment to the Intelligence Community Postdoctoral Research Fellowship Program at Stanford University administered by Oak Ridge Institute for Science and Education (ORISE) through an interagency agreement between the U.S. Department of Energy and the Office of the Director of National Intelligence (ODN). G.W. was supported by an NSF CAREER Award (IIS 1553333), a Sloan Fellowship, and a PECASE by the ARL.

Algorithm 1 D-VDAMP

Input: Sampling set Ω , wavelet transform Ψ , probability matrix \mathbf{P} , measurements \mathbf{y} , regularization parameter γ , image domain denoiser $\mathbf{D}(\mathbf{x}; \gamma\boldsymbol{\tau})$, number of iterations K_{it} .

```
1: Set  $\tilde{\mathbf{r}}_0 = \mathbf{0}$ , set  $\boldsymbol{\tau}_{-1} = \infty$ , and compute  $\mathbf{S} = |\mathbf{F}\Psi^H|^2$ 
2: for  $k = 0, 1, \dots, K_{it} - 1$  do
3:    $\mathbf{z}_k = \mathbf{y} - \mathbf{M}_\Omega \mathbf{F}\Psi^H \tilde{\mathbf{r}}_k$ 
4:    $\mathbf{r}_k = \tilde{\mathbf{r}}_k + \Psi \mathbf{F}^H \mathbf{P}^{-1} \mathbf{z}_k$ 
5:    $\boldsymbol{\tau}_k = \mathbf{S}^H \mathbf{M}_\Omega \mathbf{P}^{-1} [(\mathbf{P}^{-1} - \mathbf{1}_N) |\mathbf{z}_k|^2 + \sigma_\epsilon^2 \mathbf{1}_N]$ 
6:   if  $\|\boldsymbol{\tau}_k\|_1 > \|\boldsymbol{\tau}_{k-1}\|_1$  then
7:     break
8:   end if
9:    $\hat{\mathbf{w}}_k = \Psi \mathbf{D}(\Psi^H \mathbf{r}_k; \gamma \boldsymbol{\tau}_k)$ 
10:   $\boldsymbol{\alpha}_k = \text{M.C. estimate of } \langle \partial \Psi \mathbf{D}(\Psi^H \mathbf{r}_k; \gamma \boldsymbol{\tau}_k) \rangle_{\text{sband}}$ 
11:   $\tilde{\mathbf{r}}_{k+1} = (\hat{\mathbf{w}}_k - \boldsymbol{\alpha}_k \odot \mathbf{r}_k) \oslash (\mathbf{1}_N - \boldsymbol{\alpha}_k)$ 
12: end for
13: return  $\hat{\mathbf{x}} = \Psi^H \hat{\mathbf{w}}_k$ 
```

surements. Still, as will be demonstrated in Section 3, the performance of VDAMP trails behind that of P&P methods which can leverage far more sophisticated priors.

In this work, we propose, analyze, and test a P&P denoising-based VDAMP (D-VDAMP) algorithm which extends and substantially improves the performance of VDAMP by incorporating a novel CNN-based colored noise removal algorithm in place of soft wavelet thresholding.

2. D-VDAMP

The proposed D-VDAMP algorithm is presented in Algorithm 1 and is described below. Like the VDAMP algorithm on which it is based, D-VDAMP forms a series of noisy (\mathbf{r}_k) and denoised ($\hat{\mathbf{w}}_k$) estimates of the true signal’s wavelet coefficients, $\mathbf{w}_o = \Psi \mathbf{x}_o$, where Ψ denotes a forward wavelet transform [15]. We use a four level 2-D Haar transform throughout the paper.

On line 3 the algorithm computes the residual error between the observations \mathbf{y} and the wavelet coefficient estimate $\tilde{\mathbf{r}}_k$. On line 4, D-VDAMP uses this estimate of the residual to take a *density compensated* gradient descent step. That is, rather than taking a gradient step to reduce $\|\mathbf{y} - \mathbf{M}_\Omega(\mathbf{F}\mathbf{x})\|^2$, the algorithm instead takes a step to reduce $\mathbb{E}_\Omega \|\mathbf{y} - \mathbf{M}_\Omega(\mathbf{F}\mathbf{x})\|^2$. This step is central to whitening the effective noise within the algorithm but, because it involves scaling the residual by \mathbf{P}^{-1} , this modification makes the algorithm more sensitive to measurement noise [15].

On line 5 the algorithm computes an estimate of the variance in the wavelet domain. On lines 6–8 the algorithm compares the estimated power of the effective noise associated with the current iteration with the estimated power from the previous iteration. If the current iteration’s estimate is larger, the solution is getting worse and the algorithm terminates. On line 9 the algorithm applies an image domain denoiser. The denoiser is parameterized by the estimated diagonal, $\boldsymbol{\tau}_k$, of the effective noise’s covariance matrix and a tunable parameter, γ , which determines the amount of regularization. On

line 10 the algorithm computes a Monte Carlo estimate of the average partial derivative associated with denoising the elements of each wavelet subband. See Section 2.1 for more information.

Line 11 is the colored Onsager correction step. The intuition behind this step is that each wavelet band of the reconstruction is updated at a different rate. The lower the average partial derivative with respect to a subband (which is a proxy for the variance associated with the reconstruction in that sideband), the faster that band is updated. See [7, 15] for more information about the Onsager correction.

Finally, on line 13 the algorithm maps $\hat{\mathbf{w}}_k$ back to the image domain to form the final estimate of the image. Note, that unlike VDAMP, our algorithm does not have a final gradient descent step on line 13. The exclusion of this term significantly improved the algorithm’s performance at low SNRs, while trading off some performance at higher SNRs.

2.1. Calculating Average Partial Derivatives

A key step in the VDAMP algorithm is computing the average partial derivative across each wavelet subband, $\langle \partial \Psi \mathbf{D}(\Psi^H \mathbf{r}; \gamma \boldsymbol{\tau}) \rangle_{\text{sband}}$. In this work, we do so by extending the Monte-Carlo procedure developed in [17].

Let $g(\mathbf{r}) = \Psi \mathbf{D}(\Psi^H \mathbf{r}; \gamma \boldsymbol{\tau})$. For each subband s , we estimate the average partial derivative of the real part of $g(\mathbf{r})$ with

$$\langle \partial \mathcal{R}(g(\mathbf{r})) \rangle_{\text{sband}} \approx \frac{1}{J_s} \mathcal{R}(\mathbf{b}_s^t) \left(\frac{\mathcal{R}(g(\mathbf{r} + \eta \mathcal{R}(\mathbf{b}_s))) - g(\mathbf{r}))}{\eta} \right)$$

where $\mathcal{R}(\cdot)$ denotes taking the real part of the argument, η is a small constant (we use $\frac{1}{1000} \max(\mathbf{r})$), J_s is the number of elements in subband s , and \mathbf{b}_s is a vector whose elements within the band s follows an i.i.d. circular complex Gaussian distribution with variance 2 (real and imaginary part each have variance 1) and whose elements outside this band are 0. An analogous expression is used to compute the average partial derivative of the imaginary component. Following [15], we compute the average partial derivative of the complex function by averaging the partials from the real and imaginary parts.

2.2. Vector “State Evolution”

Within the iterations of VDAMP, the term \mathbf{r}_k can be thought of as a noisy estimate of the true wavelet coefficients $\mathbf{w}_o = \Psi \mathbf{x}_o$. The difference between these two terms, $\boldsymbol{\nu}_k = \mathbf{r}_k - \mathbf{w}_o$, is known as the effective noise. Like VDAMP, D-VDAMP comes with a (weak) state evolution framework to predict the covariance of $\boldsymbol{\nu}_k$. The state evolution finding is stated below and is empirically supported in Figure 1.

Finding 1 *The effective noise within each wavelet subband, s , follows a white Gaussian distribution with a variance equal to $\tau_{k,s}$ from line 5.*

Note that this “state evolution” differs from and is weaker than the typical AMP state evolution: The variances at iteration $k + 1$ depends on the residual \mathbf{z}_k from the previous iteration, not just the previous state evolution prediction. Accordingly, this state evolution is not self-contained and cannot be relied upon to analyze the noise sensitivity and con-

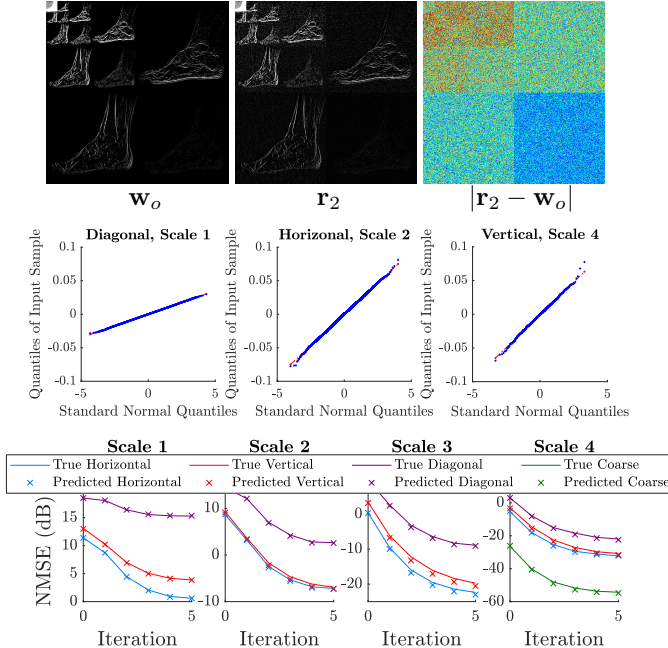


Fig. 1: State evolution. (Top) An illustration of the effective error in the wavelet domain at iteration 2 of the algorithm: Each subband exhibits a different distribution and the elements within each subband appear uncorrelated. (Middle) Quantile-quantile plots of the empirical distribution within several of the effective error subbands: Linear plots indicate a Gaussian distribution. (Bottom) The empirical variances of the error within each subband alongside the predicted variances, $\tau_{k,s}$: The variances are accurately predicted.

vergence of the algorithm, as has been done with alternative AMP frameworks, e.g., [18]. Instead, this state evolution only tells you the covariance of the effective noise at each iteration.

2.3. Removing Colored Noise

We propose a new CNN architecture which leverages the known covariance of the colored effective noise in order to remove it. Our proposed architecture is a modified version of the DnCNN [19] architecture where each intermediate feature map is concatenated with a $h \times w \times 13$ tensor where the j^{th} slice of each tensor contains $h \times w$ copies of the standard deviation associated with the j^{th} wavelet subband. (A Haar transform across 4 scales has 13 wavelet subbands.) The network architecture thereby provides all convolutional layers direct access to the standard deviations in each wavelet subband as extra channels.

Four copies of this CNN were trained to remove colored Gaussian noise that has a diagonal covariance matrix when represented in the wavelet domain. The networks were specialized for when the standard deviation of the noise across the 13 wavelet bands were uniformly distributed in the ranges 0–20, 20–50, 50–120, and 120–500, respectively. (Pixel values were in the range 0–255.) The training dataset was made of roughly 127 000 different 48×48 patches formed by cropping, scaling, flipping, and rotating 50 MRI images from the “Stanford 2D FSE” dataset available at <http://mridata.org/>, which is maintained by Miki

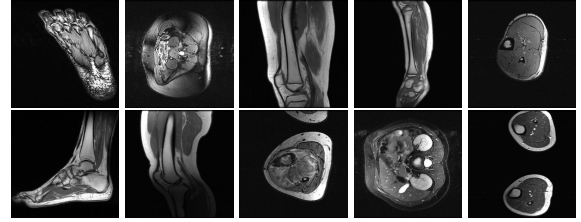


Fig. 2: Testing dataset from <http://mridata.org/>.

Lustig and collaborators. The networks was trained for 50 epochs using the ADAM optimizer with a learning rate of 0.001 and batch size of 256.

3. SIMULATION RESULTS

Dataset We test the algorithms on the 256×256 MRI images presented in Figure 2. (These images were not used to generate the training dataset.) For simplicity, our present simulations assume the signal is real-valued. The proposed method could be extended to deal with the more realistic complex-valued case by adding an extra channel to the input and output of the DnCNN denoiser, as is done in [6].

Measurements Our measurements are formed by adding i.i.d. circular complex Gaussian noise to variable density sampled Fourier coefficients of the images [20]. The variable density sampling strategy preferentially samples the low frequency components, which for MRI images generally contain more information. Extending the algorithm to other sampling strategies, such as Cartesian [6], remains future work.

Competition We compare the proposed algorithm against the wavelet-sparsity based VDAMP algorithm [15] (with a 2-D Haar basis), the total variation based TVAL3 algorithm [21], and two plug-and-play algorithms: P&P ADMM [2] and RED [4]. The latter two algorithms represent the state-of-the-art on this task [6]. Note that, while they can offer excellent performance when trained on a fixed measurement matrix, unrolled methods like ADMM-Net [22] do not generalize across measurement patterns, and so are not compared against here.

We test both plug and play algorithms with both the classical BM3D denoising algorithm [23] and the CNN-based DnCNN denoising algorithm [19], trained with white Gaussian noise. Similarly, we test the D-VDAMP algorithm with BM3D, a DnCNN network trained with white noise, a DnCNN network trained with colored noise, and our proposed, modified DnCNN network trained with colored noise. **Algorithm Parameters** VDAMP is run for 30 iterations, TVAL3 is run for 300 iterations. P&P ADMM and RED are both run for 200 iterations. D-VDAMP is run for 10 iterations or until the predicted power of the effective noise, as given by the sum of the elements of τ_k , increases.

Both P&P ADMM and RED use denoisers whose parameters were optimized to denoise noise with a standard deviation between 20–50 with DnCNN or 25 with BM3D (among the four networks, this one worked the best). The RED loss is minimized using proximal gradient descent with adaptive step sizes, as implemented by FASTA [24], and with a prox-

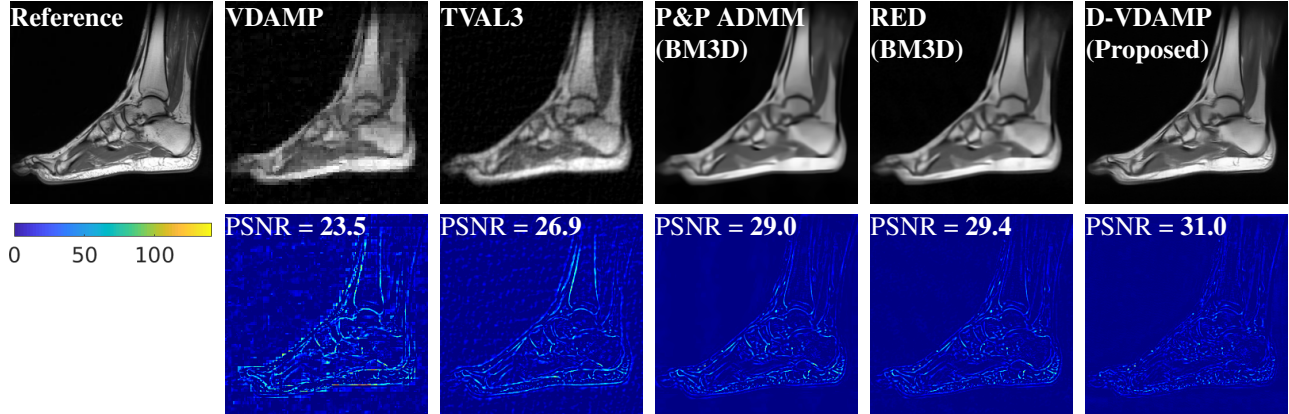


Fig. 3: 256×256 reconstructions and error maps for several algorithms from high SNR measurements with a sampling rate of $\frac{m}{n} = \frac{1}{16}$. The proposed D-VDAMP algorithm forms sharper and more accurate reconstructions than existing techniques.

Table 1: Average PSNRs (dB) and runtimes (seconds) of 256×256 reconstructions of MRI images with high SNR (40 dB) variable density Fourier measurements with various sampling rates.

Method	$\frac{m}{n} = \frac{1}{16}$		$\frac{m}{n} = \frac{1}{12}$		$\frac{m}{n} = \frac{1}{8}$		$\frac{m}{n} = \frac{1}{4}$	
	PSNR	Time	PSNR	Time	PSNR	Time	PSNR	Time
VDAMP	25.2	0.2	26.1	0.2	27.6	0.3	32.3	0.5
TVAL3	27.7	0.6	28.3	0.6	29.1	0.7	32.0	0.8
P&P ADMM (BM3D)	30.0	112.0	30.5	114.7	31.0	114.3	32.4	119.1
P&P ADMM (DnCNN, white)	27.6	7.3	28.9	7.4	30.7	7.4	33.6	7.5
RED (BM3D)	30.3	284.1	30.7	282.9	31.4	281.8	33.2	287.9
RED (DnCNN, white)	28.8	13.2	29.9	12.9	31.2	12.8	34.3	12.4
D-VDAMP (BM3D)	28.4	62.4	30.2	98.0	32.5	121.0	39.9	157.0
D-VDAMP (DnCNN, white)	29.3	2.9	29.1	4.1	30.0	4.4	32.8	5.3
D-VDAMP (DnCNN, colored)	29.8	2.9	31.5	4.1	33.5	4.4	38.3	5.3
D-VDAMP (Proposed)	31.4	3.1	34.0	4.1	36.4	5.9	41.3	6.1

Table 2: Average PSNRs (dB) of 256×256 reconstructions of MRI images sampled with variable density Fourier measurements at a rate of $\frac{m}{n} = \frac{1}{8}$ under various SNRs.

Method	SNR = 25dB	SNR = 20dB	SNR = 15dB	SNR = 10dB	SNR = 5dB
	PSNR	PSNR	PSNR	PSNR	PSNR
P&P ADMM (BM3D)	30.9	30.8	30.7	30.2	27.8
RED (BM3D)	31.4	31.1	30.6	29.3	25.0
D-VDAMP (BM3D)	32.8	31.8	30.1	27.5	25.0
D-VDAMP (Proposed)	34.8	33.0	30.8	28.0	25.0

imal mapping step that applies the denoiser only once. P&P ADMM’s ρ and γ parameters, as defined in [25], are both set to 1. RED’s λ parameter is also set to 1. D-VDAMP’s γ parameter is set to 0.75. All the P&P algorithms denoise only the real part of the signal. P&P ADMM and RED simply zero out the imaginary part while D-VDAMP instead scales the imaginary part by 0.1, so as to maintain a nonzero average partial derivative.

Results Table 1 demonstrates that when dealing with high SNR measurements, the proposed algorithm substantially outperforms the state-of-the-art. It outperforms wavelet based methods by nearly 10 dB and uniformly outperforms other P&P methods by at least 1 dB. As illustrated in Figure 3, the proposed algorithm results in reconstructions with fewer artifacts and sharper edges.

However, as noted in [15], the density compensated gradient step of VDAMP (line 4), which multiplies \mathbf{z}_k by \mathbf{P}^{-1} ,

makes D-VDAMP sensitive to measurement noise. Accordingly, as demonstrate in Table 2, at lower SNRs existing P&P algorithms outperform D-VDAMP.

4. DISCUSSION

A chief criticism against many learning-based reconstruction methods is that they can produce realistic looking images, even when the measurements contain little information about the actual scene [26]. These images can lead practitioners to trust the reconstruction, even when they should not. Fortunately, because the last step of D-VDAMP is equivalent to removing colored Gaussian noise with known covariance from the ground-truth signal, Stein’s unbiased risk estimate can be combined with D-VDAMP to produce heat maps of the expected squared error per pixel associated with the reconstruction [27, 28, 29]. This allows practitioners to judge which portions of the reconstruction can be trusted.

5. REFERENCES

- [1] A. Danielyan, A. Foi, V. Katkovnik, K. Egiazarian, and P. Milanfar, "Spatially adaptive filtering as regularization in inverse imaging: Compressive sensing super-resolution and upsampling," *Super-Resolution Imaging*, pp. 123–154, 2010.
- [2] Singanallur V Venkatakrishnan, Charles A Bouman, and Brendt Wohlberg, "Plug-and-play priors for model based reconstruction," in *2013 IEEE Global Conference on Signal and Information Processing*. IEEE, 2013, pp. 945–948.
- [3] Christopher A Metzler, Arian Maleki, and Richard G Baraniuk, "From denoising to compressed sensing," *IEEE Transactions on Information Theory*, vol. 62, no. 9, pp. 5117–5144, 2016.
- [4] Yaniv Romano, Michael Elad, and Peyman Milanfar, "The little engine that could: Regularization by denoising (red)," *SIAM Journal on Imaging Sciences*, vol. 10, no. 4, pp. 1804–1844, 2017.
- [5] Christopher A. Metzler, Ali Mousavi, and Richard Baraniuk, "Learned d-amp: Principled neural network based compressive image recovery," in *Advances in Neural Information Processing Systems*, 2017, pp. 1772–1783.
- [6] Rizwan Ahmad, Charles A Bouman, Gregory T Buzzard, Stanley Chan, Sizhou Liu, Edward T Reehorst, and Philip Schniter, "Plug and play methods for magnetic resonance imaging (long version)," *arXiv preprint arXiv:1903.08616*, 2019.
- [7] David L Donoho, Arian Maleki, and Andrea Montanari, "Message-passing algorithms for compressed sensing," *Proceedings of the National Academy of Sciences*, vol. 106, no. 45, pp. 18914–18919, 2009.
- [8] Philip Schniter, Sundeep Rangan, and Alyson Fletcher, "Denoising based vector approximate message passing," *arXiv preprint arXiv:1611.01376*, 2016.
- [9] Sundeep Rangan, Philip Schniter, Alyson K Fletcher, and Subrata Sarkar, "On the convergence of approximate message passing with arbitrary matrices," *IEEE Transactions on Information Theory*, vol. 65, no. 9, pp. 5339–5351, 2019.
- [10] Francesco Caltagirone, Lenka Zdeborová, and Florent Krzakala, "On convergence of approximate message passing," in *2014 IEEE International Symposium on Information Theory*. IEEE, 2014, pp. 1812–1816.
- [11] Andre Manoel, Florent Krzakala, Eric Tramel, and Lenka Zdeborova, "Swept approximate message passing for sparse estimation," in *International Conference on Machine Learning*, 2015, pp. 1123–1132.
- [12] Sundeep Rangan, Philip Schniter, and Alyson K Fletcher, "Vector approximate message passing," *IEEE Transactions on Information Theory*, vol. 65, no. 10, pp. 6664–6684, 2019.
- [13] Junjie Ma and Li Ping, "Orthogonal amp," *IEEE Access*, vol. 5, pp. 2020–2033, 2017.
- [14] Ender M Eksioğlu and A Korhan Tanc, "Denoising amp for mri reconstruction: Bm3d-amp-mri," *SIAM Journal on Imaging Sciences*, vol. 11, no. 3, pp. 2090–2109, 2018.
- [15] Charles Millard, Aaron T Hess, Boris Mailhé, and Jared Tanner, "Approximate message passing with a colored aliasing model for variable density fourier sampled images," *arXiv preprint arXiv:2003.02701*, 2020.
- [16] Philip Schniter, Sundeep Rangan, and Allison K. Fletcher, "Plug-and-play image recovery using vector amp," 2017, presented at Proc. Intl. Biomed. Astronom. Signal Process. (BASP) Frontiers Workshop, Villars-sur-Ollon, Switzerland (available at http://www2.ece.ohio-state.edu/~schniter/pdf/baspl7_poster.pdf).
- [17] Sathish Ramani, Thierry Blu, and Michael Unser, "Monte-carlo sure: A black-box optimization of regularization parameters for general denoising algorithms," *IEEE Transactions on image processing*, vol. 17, no. 9, pp. 1540–1554, 2008.
- [18] David L Donoho, Arian Maleki, and Andrea Montanari, "The noise-sensitivity phase transition in compressed sensing," *IEEE Transactions on Information Theory*, vol. 57, no. 10, pp. 6920–6941, 2011.
- [19] Kai Zhang, Wangmeng Zuo, Yunjin Chen, Deyu Meng, and Lei Zhang, "Beyond a gaussian denoiser: Residual learning of deep cnn for image denoising," *IEEE Transactions on Image Processing*, vol. 26, no. 7, pp. 3142–3155, 2017.
- [20] Michael Lustig, David Donoho, and John M Pauly, "Sparse mri: The application of compressed sensing for rapid mr imaging," *Magnetic Resonance in Medicine: An Official Journal of the International Society for Magnetic Resonance in Medicine*, vol. 58, no. 6, pp. 1182–1195, 2007.
- [21] Chengbo Li, Wotao Yin, and Yin Zhang, "User's guide for TVAL3: TV minimization by augmented Lagrangian and alternating direction algorithms," *Rice CAAM Department report*, vol. 20, pp. 46–47, 2009.
- [22] Jian Sun, Huibin Li, Zongben Xu, et al., "Deep admm-net for compressive sensing mri," in *Advances in neural information processing systems*, 2016, pp. 10–18.
- [23] Kostadin Dabov, Alessandro Foi, Vladimir Katkovnik, and Karen Egiazarian, "Image denoising by sparse 3-d transform-domain collaborative filtering," *IEEE Transactions on image processing*, vol. 16, no. 8, pp. 2080–2095, 2007.
- [24] Tom Goldstein, Christoph Studer, and Richard Baraniuk, "A field guide to forward-backward splitting with a fasta implementation," *arXiv preprint arXiv:1411.3406*, 2014.
- [25] Stanley H Chan, Xiran Wang, and Omar A Elgendy, "Plug-and-play admm for image restoration: Fixed-point convergence and applications," *IEEE Transactions on Computational Imaging*, vol. 3, no. 1, pp. 84–98, 2016.
- [26] Nina M Gottschling, Vegard Antun, Ben Adcock, and Anders C Hansen, "The troublesome kernel: why deep learning for inverse problems is typically unstable," *arXiv preprint arXiv:2001.01258*, 2020.
- [27] Charles-Alban Deledalle, Vincent Duval, and Joseph Salmon, "Non-local methods with shape-adaptive patches (nlm-sap)," *Journal of Mathematical Imaging and Vision*, vol. 43, no. 2, pp. 103–120, 2012.
- [28] Vineet Edupuganti, Morteza Mardani, Shreyas Vasawala, and John Pauly, "Uncertainty quantification in deep mri reconstruction," *IEEE Transactions on Medical Imaging*, 2020.
- [29] Ruangrawee Kitichotkul, Christopher A. Metzler, Frank Ong, and Gordon Wetzstein, "Suremap: Predicting uncertainty in cnn-based image reconstructions using Stein's unbiased risk estimate," *Under Review*.